


# Real-time, *in situ* probing of gamma radiation damage with packaged integrated photonic chips

QINGYANG DU,<sup>1</sup>  JÉRÔME MICHON,<sup>1</sup> BINGZHAO LI,<sup>2</sup> DEREK KITA,<sup>1</sup>  DANHAO MA,<sup>1</sup> HAIJIE ZUO,<sup>1</sup>   
SHAOLIANG YU,<sup>1</sup>  TIAN GU,<sup>1</sup> ANURADHA AGARWAL,<sup>1</sup> MO LI,<sup>2,3</sup>  AND JUEJUN HU<sup>1,\*</sup>

<sup>1</sup>Department of Materials Science & Engineering, Massachusetts Institute of Technology, Cambridge, Massachusetts 02139, USA

<sup>2</sup>Department of Electrical and Computer Engineering, University of Washington, Seattle, Washington 98195, USA

<sup>3</sup>Department of Physics, University of Washington, Seattle, Washington 98195, USA

\*Corresponding author: [hujuejun@mit.edu](mailto:hujuejun@mit.edu)

Received 2 October 2019; revised 25 November 2019; accepted 3 December 2019; posted 4 December 2019 (Doc. ID 379019); published 31 January 2020

Integrated photonics is poised to become a mainstream solution for high-speed data communications and sensing in harsh radiation environments, such as outer space, high-energy physics facilities, nuclear power plants, and test fusion reactors. Understanding the impact of radiation damage in optical materials and devices is thus a prerequisite to building radiation-hard photonic systems for these applications. In this paper, we report real-time, *in situ* analysis of radiation damage in integrated photonic devices. The devices, integrated with an optical fiber array package and a baseline-correction temperature sensor, can be remotely interrogated while exposed to ionizing radiation over a long period without compromising their structural and optical integrity. We also introduce a method to deconvolve the radiation damage responses from different constituent materials in a device. The approach was implemented to quantify gamma radiation damage and post-radiation relaxation behavior of SiO<sub>2</sub>-cladded SiC photonic devices. Our findings suggest that densification induced by Compton scattering displacement defects is the primary mechanism for the observed index change in SiC. Additionally, post-radiation relaxation in amorphous SiC does not restore the original pre-irradiated structural state of the material. Our results further point to the potential of realizing radiation-hard photonic device designs taking advantage of the opposite signs of radiation-induced index changes in SiC and SiO<sub>2</sub>. © 2020 Chinese Laser Press

<https://doi.org/10.1364/PRJ.379019>

## 1. INTRODUCTION

Over the past decade, integrated photonics has rapidly been established as the technology of choice over electronics for applications covering long-haul data communications [1], radio-frequency photonics [2], and on-chip spectroscopic sensing [3]. Devices for operation in harsh radiation environments are yet another arena where integrated photonics presents unique advantages. Integrated photonic modules are being deployed in these settings for applications including optical links for high-volume high-energy physics data transmission [4] and satellite communications [5]. In addition to their inherent advantages in energy-efficient data communications and remote sensing/imaging, recent studies have revealed that various radiation-hard integrated photonic components can be realized with proper designs [6–9].

To enable such radiation-hard designs, it is essential to develop a thorough understanding of the radiation-induced effects in relevant photonic materials and devices. Toward this goal, several studies have been undertaken to evaluate the effects in integrated photonic devices [10–14]. In these studies,

responses of the devices to ionizing radiations were only quantified *ex situ*, i.e., after the devices were removed from the irradiation chamber. On the other hand, *in situ* monitoring of radiation damage has also been reported in silicon-on-insulator micro-ring resonators (under gamma ray irradiation) [15] and Mach–Zehnder interferometers (under X-ray and neutron irradiation) [16,17]. Such measurements allow for real-time monitoring of the kinetics of radiation damage as well as post-radiation relaxation, which takes place at room temperature and commences immediately after irradiation concludes [18,19].

A standing challenge, however, is that only radiation-induced changes of the overall device response were reported in these studies, and it is unclear which constituent materials are responsible for the performance variation and to what extent. For instance, in an optical waveguide, both the core and cladding materials influence its optical properties; elucidating their respective relative contributions can open up engineering spaces for radiation-hard designs, as we shall discuss later. It is therefore imperative to identify a technique to deconvolve the radiation-induced responses of individual constituent materials.

In this study, we seek to address the challenge by performing real-time measurements of photonic device arrays while they were being irradiated *in situ*. Stable long-term measurements were made possible by packaging the devices with optical fiber arrays (FAs) as a robust optical interface for light input/output coupling. We further leverage the FAs to facilitate parallel characterization of multiple waveguide devices on the same chip. The devices, each designed with a different geometric dimension, give rise to distinctive field distributions in the core and cladding materials. The difference in their radiation-induced responses was then used to isolate the property changes of the core and cladding materials.

## 2. DEVICE FABRICATION AND PACKAGING

Specifically, we employ SiC/SiO<sub>2</sub> as the model system to demonstrate our approach. SiC, which consists of a robust 3D covalent atomic network interconnected through strong Si-C bonds, has long been regarded as a leading material candidate for radiation-hard devices [20]. Recently, there has been a surge of interest in SiC for integrated photonics applications covering non-linear optics, optomechanics, and quantum optics [20–34]. In our study, we choose amorphous SiC (a-SiC) deposited using plasma-enhanced chemical vapor deposition (PECVD) as the material platform. The choice of PECVD SiC as the waveguide core material is mainly justified by its CMOS compatibility and ease of processing [21,22], as neither wafer bonding (in the case of SiC-on-insulator) [23–25] nor undercut etching for suspended structures (in the case of epitaxial SiC-on-Si) [26–34] is needed. The devices were fabricated

on piranha cleaned Si wafers. The process started with growing a 2- $\mu\text{m}$ -thick PECVD SiO<sub>2</sub> under cladding layer. A 275-nm film of amorphous silicon carbide was deposited subsequently via PECVD with a gas mixture of CH<sub>4</sub> and SiH<sub>4</sub> following previously published conditions [22]. Patterning of the SiC film was conducted on an Elionix ELS-F125 electron beam lithography (EBL) tool with a beam current of 10 nA and an optimized dose of 3200  $\mu\text{C}/\text{cm}^2$ . 6% hydrogen silsesquioxane was chosen as the EBL resist as it provides optimal etching resistivity. The chip was then developed in 25% tetramethylammonium hydroxide for 2.5 min to reveal the pattern. Reactive ion etching was performed in an STS inductively coupled plasma reactive ion etching tool (ICP-RIE) with a forward power of 1000 W and an etching gas of Cl<sub>2</sub> at a pressure of 30 mTorr. These parameters yielded an etching rate of a-SiC at 600 nm/min. Device fabrication was completed by depositing another 2- $\mu\text{m}$  PECVD oxide layer as the top cladding. The devices fabricated following the protocols are symmetrically cladded with PECVD SiO<sub>2</sub>. The cross-sectional dimensions of the waveguides were quantified using scanning electron microscopy and used as input parameters for full-vectorial optical modal simulations. In device packaging, the as-fabricated devices were packaged with optical fiber arrays (SQS Vlaknova Optika) using UV curable epoxy (Masterbond UV15TK) as the bonding agent. Fibers with an incident angle of 15° were first actively aligned to the on-chip grating couplers to maximize the transmitted power. Epoxy was applied onto the chip to securely bond the fibers to the chip. The active alignment was repeated after epoxy application to ensure optimal coupling. The epoxy was then cured through flood UV exposure.

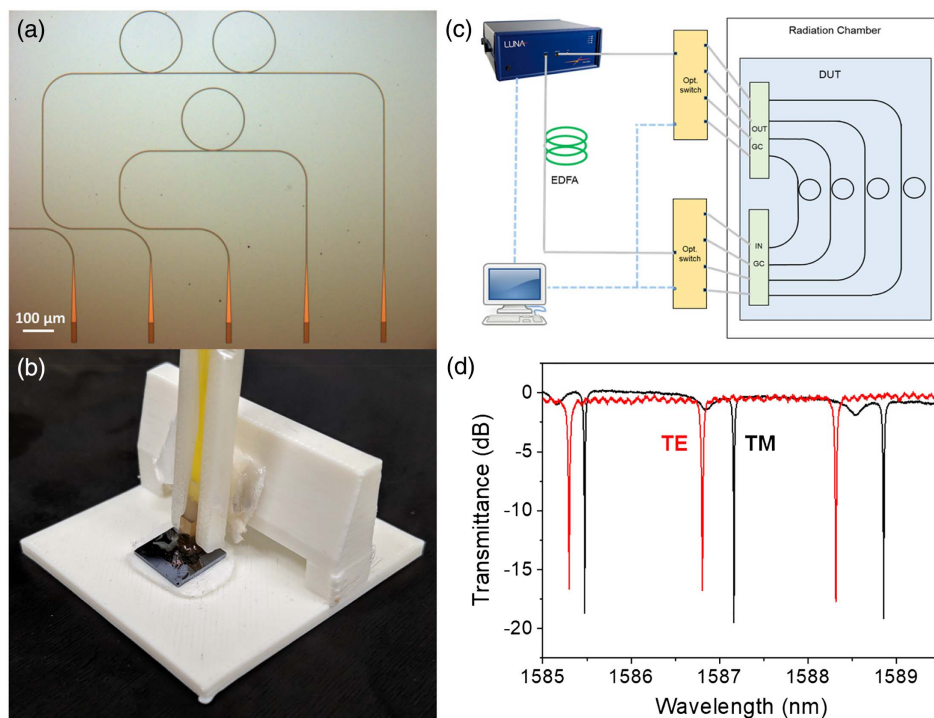


**Fig. 1.** (a) Top-view micrograph of the photonic chip showing the micro-ring resonators and the grating couplers; (b) photograph of the packaged photonic chip; (c) block diagram showing the *in situ* measurement setup. EDFA, erbium-doped fiber amplifier; GC, grating coupler; Opt. switch, optical switch; DUT, device under test. (d) Normalized transmittance spectra of a micro-ring resonator under test for both TE- and TM-polarized modes.

After the epoxy was fully cured, the fibers were released from the alignment stage and attached to a custom-designed and 3D printed device holder. A thermal couple is also bonded onto the chip for *in situ* temperature monitoring. Figure 1(b) shows an image of the packaged photonic chip. Prior to irradiation, the temperature-dependent wavelength shifts of the SiC resonator devices under test were quantified and used to correct the resonance drift due to ambient temperature fluctuations during the experiment. The fiber-tethered devices were then loaded into a GammaCell Co-60 Irradiator and exposed to a gamma ray dose rate of approximately 4000 rad/min (calibrated with respect to Si). Transmittance spectra of both transverse electric (TE) and transverse magnetic (TM) polarizations were recorded concurrently using an optical vector analyzer (LUNA Technologies OVA-5000) with a built-in external cavity tunable laser. Figure 1(c) depicts a block diagram illustrating the testing setup and a representative set of measured TE/TM spectra is shown in Fig. 1(d).

### 3. IN SITU RADIATION STUDY

Long-term stability of the fiber package under gamma irradiation was experimentally confirmed by examining the loop-back insertion loss variation in the *in situ* experiment. As is shown in Fig. 2(a), changes of the insertion losses remain negligible up to a large irradiation dose of 10 Mrad and are consistently less than the device-to-device variation. On the device side, gamma ray irradiation resulted in progressive

resonant wavelength shifts with increasing dose [Fig. 2(b)]. The observed resonant wavelength shift was a combined effect of radiation-induced refractive index changes in the SiC core ( $\Delta n_{\text{core}}$ ) and SiO<sub>2</sub> cladding ( $\Delta n_{\text{clad}}$ ). To elucidate the respective contributions from the core and cladding, micro-ring resonators with different core widths (from 700 nm to 1000 nm) but otherwise identical configurations (275 nm core height, 150  $\mu\text{m}$  diameter) were fabricated on the same chip. Waveguides with different dimensions give rise to varying confinement factors  $\Gamma_{\text{core}}$  and  $\Gamma_{\text{clad}}$  in the core and cladding regions, respectively. The measured resonant wavelength drift  $\Delta\lambda$  relates to the modal effective index change caused by irradiation  $\Delta n_{\text{eff}}$  through

$$\Delta\lambda = \frac{\Delta n_{\text{eff}}}{n_g} \cdot \lambda = (\Gamma_{\text{core}} \Delta n_{\text{core}} + \Gamma_{\text{clad}} \Delta n_{\text{clad}}) \cdot \frac{\lambda}{n_g}. \quad (1)$$

Here  $\lambda$  denotes the starting resonant wavelength and  $n_g$  is the group index. It is important to note that  $\Gamma_{\text{core}}$  and  $\Gamma_{\text{clad}}$  in general do not add up to unity due to the slow light effect [35]. We define normalized confinement factors as follows:

$$\Gamma_{\text{norm,core}} = \frac{\Gamma_{\text{core}}}{\Gamma_{\text{core}} + \Gamma_{\text{clad}}} \quad \text{and} \quad \Gamma_{\text{norm,clad}} = \frac{\Gamma_{\text{clad}}}{\Gamma_{\text{core}} + \Gamma_{\text{clad}}}. \quad (2)$$

We see that the sum of the so-defined  $\Gamma_{\text{norm,core}}$  and  $\Gamma_{\text{norm,clad}}$  always equals unity. Equation (1) can then be cast in the following form:

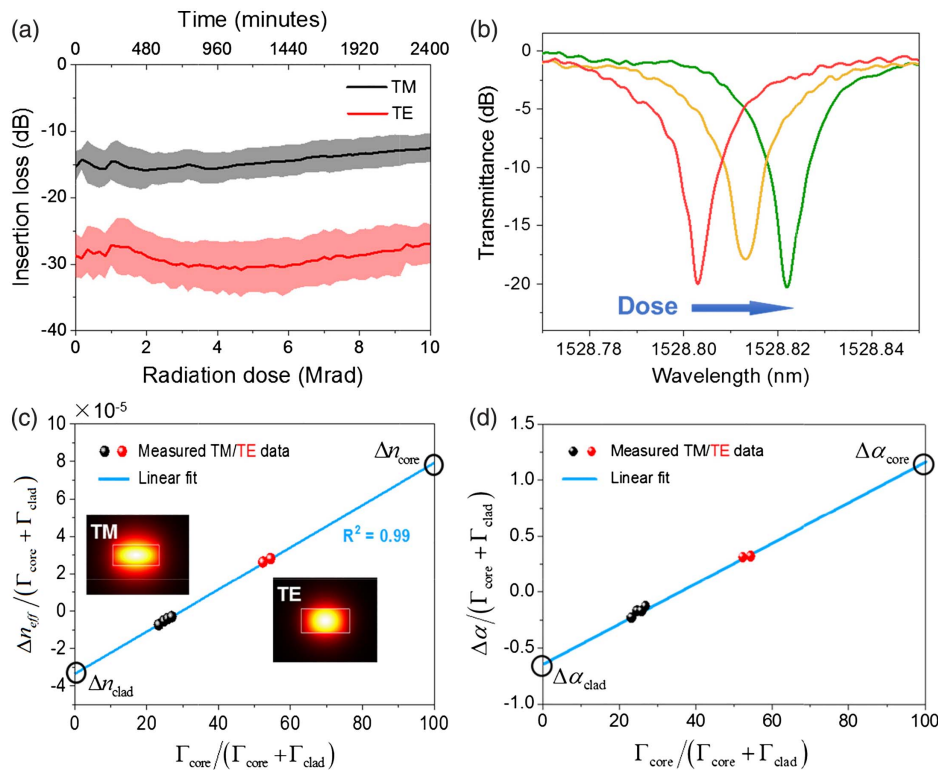


**Fig. 2.** (a) Insertion loss change of the fiber-packaged chip during *in situ* irradiation: here the error bars (shaded regions) are defined as the device-to-device variations on the same chip; (b) resonance shift due to gamma irradiation; the three spectra correspond to 0, 3.6 Mrad, and 8.4 Mrad radiation doses, respectively; (c) extracting material index changes from device measurements following protocols described in the text. The insets show TE- and TM-polarized waveguide mode profiles for SiC waveguides; (d) extracting material loss change from device measurement.

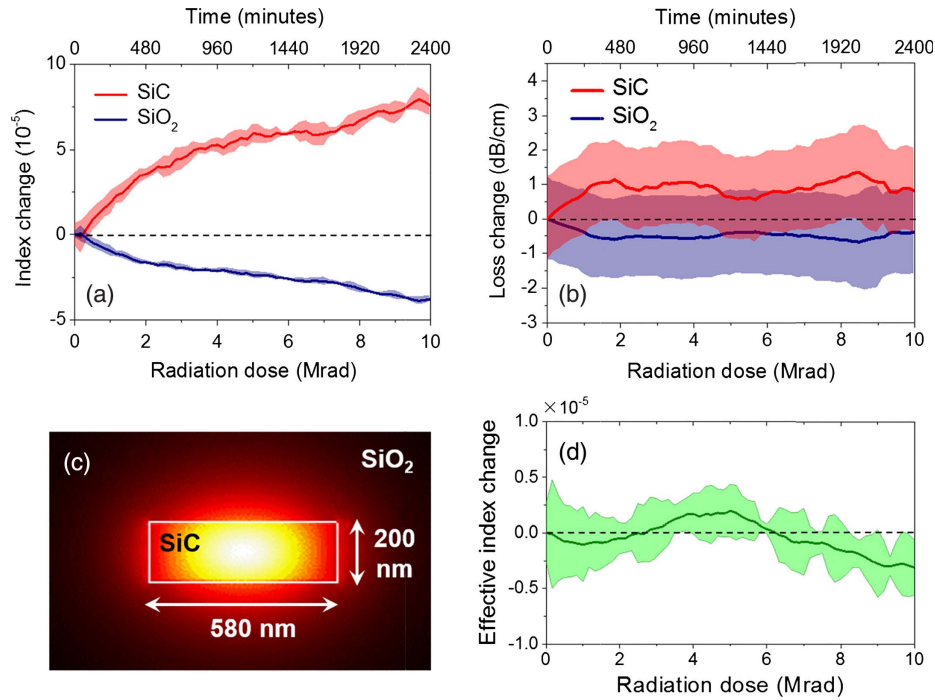


**Fig. 3.** *In situ* measured changes of (a) refractive indices and (b) optical losses in SiC and SiO<sub>2</sub> induced by gamma ray irradiation; (c) TE mode intensity profile of the radiation-hard SiC waveguide device design; (d) projected TE-mode effective index change of the design in (c) based on measurement data in (a). The shaded regions in (a), (b), and (d) denote standard deviations of data taken on multiple devices on the same chip.

$$\begin{aligned} \frac{\Delta n_{\text{eff}}}{\Gamma_{\text{core}} + \Gamma_{\text{clad}}} &= \Gamma_{\text{norm,core}} \Delta n_{\text{core}} + (1 - \Gamma_{\text{norm,core}}) \Delta n_{\text{clad}} \\ &= (\Delta n_{\text{core}} - \Delta n_{\text{clad}}) \Gamma_{\text{norm,core}} + \Delta n_{\text{clad}}. \end{aligned} \quad (3)$$

Equation (3) suggests that the measured  $\Delta n_{\text{eff}}/(\Gamma_{\text{core}} + \Gamma_{\text{clad}})$  for all the resonators and polarizations at a given radiation dose, when plotted as a function of  $\Gamma_{\text{norm,core}}$ , should fall on a straight line. As is seen in an example shown in Fig. 2(c), this is indeed the case and linear fits of our measured data consistently give coefficients of determination ( $R^2$ ) above 0.99. The intercepts of the fitted line with  $\Gamma_{\text{norm,core}} = 1$  and  $\Gamma_{\text{norm,core}} = 0$  then correspond to  $\Delta n_{\text{core}}$  and  $\Delta n_{\text{clad}}$ , respectively, with the particular radiation dose.

Besides inferring the index changes of core and cladding materials, the same notion can also be applied to extract the optical loss variations in both materials from the quality factor ( $Q$ -factor) modifications of the different resonator devices and polarizations and is shown in Fig. 2(d). The detailed formalism of the extraction procedure is presented in Appendix A.

Figures 3(a) and 3(b) plot the radiation-dose-dependent changes in material refractive indices and optical losses, respectively. Optical losses in the materials hardly changed within the measurement error throughout the course of the irradiation experiment. The relatively large spread in the measured optical losses (approximately  $\pm 1$  dB/cm) is attributed to inherent scattering loss variations in micro-ring resonators [36]. In contrast, refractive index changes ranging from  $10^{-5}$  to  $10^{-4}$  were unambiguously quantified taking advantage of the extreme precision afforded by resonant cavity refractometry [37–39]. This index drift is sufficiently small to be negligible for most guided

wave devices. However, in devices sensitive to optical phase variations, such as Mach–Zehnder interferometers and resonators, this index drift must be properly compensated. It is also interesting to note that SiC and SiO<sub>2</sub> exhibit index changes with opposing signs. This observation implies the possibility of creating radiation-hard optical devices by engineering modal confinement to nullify the effective index drift. One such hypothetical design is illustrated in Fig. 3(c), and the projected dose-dependent effective index change of the device is plotted in Fig. 3(d) based on the measured index change values in Fig. 3(a). The design predicts waveguide effective index drift of less than  $2 \times 10^{-6}$ , more than an order of magnitude smaller than the index changes of SiC or SiO<sub>2</sub> alone. Such a design is useful in improving phase stability of photonic components in radiation environments.

The packaged device also facilitates real-time tracking of the materials' post-radiation relaxation response at room temperature. Figures 4(a) and 4(b) plot the index and loss relaxation behavior of SiC and SiO<sub>2</sub> after 10-Mrad irradiation. While the loss variation is insignificant, we observed considerable index change in SiC. Remarkably, the post-radiation index change in SiC over time is non-monotonic, showing an initial increase followed by a decrease. This is in contrast to the refractive index relaxation in crystalline Si, which occurs immediately after irradiation and always rescinds the index change induced by radiation [15].

## 4. DISCUSSION

The results from our *in situ* measurement outlined above provide important insights into the mechanism of radiation

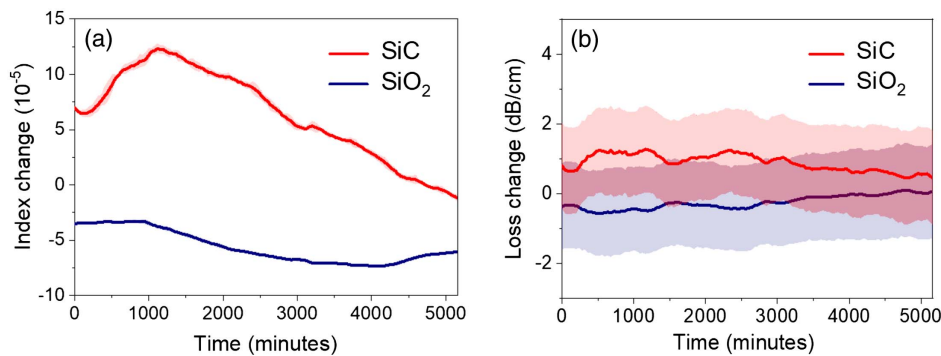


**Fig. 4.** Post-irradiation relaxation of (a) refractive indices and (b) optical losses in SiC and SiO<sub>2</sub>. The shaded regions in (b) denote standard deviations of data taken on multiple devices on the same chip.

damage in a-SiC for photonic applications. In general, there are three possible damage mechanisms caused by gamma radiation which can lead to optical property modifications: (1) ionizing radiations generate electron and hole pairs which introduce free carrier absorption and refractive index change through the plasmon dispersion effect [40]; (2) high-energy photons or particles can catalyze oxidation reactions. For instance, gamma radiation was reported to induce surface oxidation and refractive index change in SiN and a-Si when the samples were exposed to an ambient environment [11]; and (3) while direct momentum transfer from the photons of gamma rays to atoms is minimal, high-energy electrons emitted through the Compton scattering process can collide with atoms and produce point (displacement) defects [41]. Formation of these point defects further triggers a drastic rise in local temperature and pressure, which prompts local network configuration and density change in an amorphous material [42].

Here we argue that volume compaction due to Compton scattering displacement is the main mechanism responsible for the observed change in SiC. In a-SiC, the free carrier effects are negligible due to low carrier concentration and their mobility. In addition, the persistent index change after the removal of the sample from the irradiation chamber can hardly be accounted for by free carrier effects. Our SiC devices are entirely encapsulated in a SiO<sub>2</sub> cladding and isolated from the ambient atmosphere. Moreover, to identify possible radiation-induced

chemical modifications in a-SiC, we performed secondary ion mass spectroscopy (SIMS) analysis on a-SiC thin films before and after 10-Mrad total dose gamma irradiation. As is evident from Fig. 5, PECVD-deposited a-SiC film contains a high concentration of H, which is instrumental in passivating the dangling bond defects in amorphous Group IV semiconductors. An increasing oxygen concentration near the film surface indicates in-diffusion of oxygen causing surface oxidation. However, the composition profile remains identical before and after gamma irradiation, suggesting that surface oxidation is self-terminating even in uncapped a-SiC films.

To further reinforce the argument, we computed the atomic displacement parameters in SiC and the results are summarized in Table 1. Details of the calculations are furnished in Appendix A. The calculated maximum atomic recoil energies are significantly larger than the displacement energy threshold in a-SiC (13 eV [43]), and thus the Compton scattered electrons have a high probability of causing displacement damage in the material. The total density of displacement defects is approximately  $5.8 \times 10^{14} \text{ cm}^{-3}$ , or  $5.8 \times 10^{-9}$  per atomic site. The heat and pressure spikes produced by each displacement defect can impact a large number of nearby atoms [42] and remove excess free volume in as-deposited a-SiC through local bond rearrangement, thereby leading to the refractive index change.

To account for the non-monotonic relaxation behavior, we note that unlike crystalline materials, the structure of

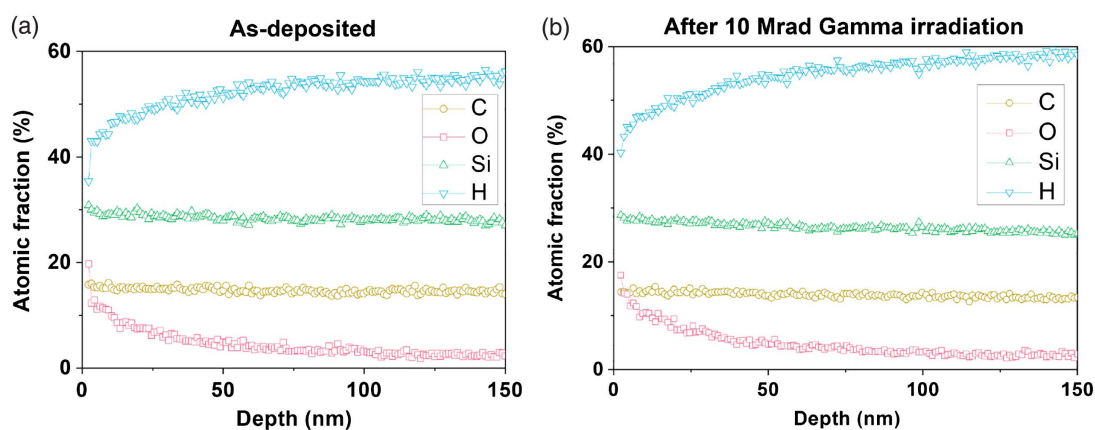


**Fig. 5.** SIMS elemental depth profiles of (a) as-deposited and (b) irradiated a-SiC films.

**Table 1. Calculated Displacement Damage Parameters in a-SiC at 10 Mrad Radiation Dose**

Atom Type	Maximum Recoil Energy (eV)	Compton Scattering		Gamma Photon Fluence (cm <sup>-2</sup> )	Atomic Density (cm <sup>-3</sup> )	Density of Displacement Defects (cm <sup>-3</sup> )
		Displacement Cross Section (Barn, 10 <sup>-22</sup> cm <sup>2</sup> )				
Silicon (Si)	204	0.45		1.9 × 10 <sup>16</sup>	6.6 × 10 <sup>22</sup>	5.6 × 10 <sup>14</sup>
Carbon (C)	476	0.28		1.9 × 10 <sup>16</sup>	3.4 × 10 <sup>22</sup>	1.8 × 10 <sup>14</sup>

amorphous compounds is characterized by a large number of metastable configurations or metabasins [44]. Structural relaxation in amorphous materials is therefore an inherently complex process and does not necessarily retrace back to the starting structural state [45]. Moreover, since the a-SiC deposited by PECVD is heavily hydrogenated, the structural relaxation kinetics may be further complicated by hydrogen diffusion, which can contribute to generation or passivation of broken (dangling) bonds in a-SiC and stabilize metastable structural configurations after irradiation [46]. The exact structural origin of the post-radiation relaxation behavior will be a topic worthy of further investigations.

## 5. CONCLUSION

In conclusion, in this study, we developed a method to probe optical property changes of photonic materials induced by ionizing radiations through *in situ* photonic device measurements. We show that the photonic package is stable in the gamma radiation environment and permits long-term, real-time measurements up to a large radiation dose. The radiation-induced refractive index change in SiC is attributed to volume compaction resulting from displacement defects generated by Compton scattered electrons. We also observed a non-monotonic variation of the SiC material refractive index during room-temperature post-radiation relaxation. Finally, findings from the study further point to the potential of realizing radiation-hard passive photonic devices leveraging the opposite signs of radiation-induced refractive index changes in different materials.

## APPENDIX A

### 1. Section I—Measurement of Radiation-Induced Material Loss

Propagation loss of a resonator can be experimentally evaluated with known resonant peak extinction ratio and the quality factor ( $Q$ ). The on-resonance power transmitted through the output end of the bus waveguide in decibel is [47]

$$T(\text{dB}) = 10 \log_{10} \frac{(\sqrt{A} - \sqrt{1 - |\kappa|^2})^2}{(1 - \sqrt{A} \cdot \sqrt{1 - |\kappa|^2})^2}, \quad (\text{A1})$$

where  $\kappa$  is the amplitude coupling coefficient between the resonator and bus waveguide, and  $A$  is the normalized amplitude of light after traveling one round trip around the resonator.  $A$  is related to waveguide linear loss  $\alpha$  by

$$\alpha = -\frac{\ln A}{L}. \quad (\text{A2})$$

We follow the generalized coupling matrix formalism [48] to analytically solve  $A$  and  $\kappa$  and determine the waveguide loss  $\alpha$ .

Given the small index change, waveguide roughness scattering loss is assumed to be constant during irradiation. The waveguide loss change is then given by

$$\Delta\alpha = (\Gamma_{\text{core}}\Delta\alpha_{\text{core}} + \Gamma_{\text{clad}}\Delta\alpha_{\text{clad}}), \quad (\text{A3})$$

where  $\Delta\alpha_{\text{core}}$  and  $\Delta\alpha_{\text{clad}}$  correspond to the material loss changes in a-SiC and SiO<sub>2</sub> materials, respectively.  $\Delta\alpha_{\text{core}}$  and  $\Delta\alpha_{\text{clad}}$  can be derived from the measured loss variations of waveguides with different cross-sectional dimensions following the same principle as the material refractive index quantification. Specifically,  $\Delta\alpha_{\text{core}}$  and  $\Delta\alpha_{\text{clad}}$  are extracted by performing a linear fit of normalized modal loss changes against normalized confinement factors for different waveguide geometries and polarizations and extrapolating the line to normalized confinement factor values of 1 and 0, respectively. It is worth noting that the error bar of the loss quantification is significantly larger than that of index measurement because of the intrinsic dispersion of  $Q$ -factors in waveguide resonator devices.

### 2. Section II—Displacement Defect Parameters in Gamma-Irradiated a-SiC

The dose rate of the gamma irradiator used in our experiment is calibrated with respect to Si. The total fluence  $\Phi$  of gamma photons is related to the radiation dose  $D$  via [49]

$$D = E_{\gamma}\Phi(\mu/\rho), \quad (\text{A4})$$

where  $E_{\gamma}$  is the average gamma photon energy of 1.24 MeV and  $\mu/\rho$  is the mass absorption coefficient equaling 0.02652 for Si [50]. Substituting the numbers into Eq. (A4), we obtain a gamma fluence of  $1.9 \times 10^{16}$  cm<sup>-2</sup> for 10 Mrad (Si) total cumulative dose.

To estimate the maximum recoil energy of atoms after collision with Compton scattered electrons, we assume that the 1.24 MeV energy of gamma photons is completely transferred to electrons. As the electron energy is considerably larger than the electron rest mass, we must use the relativistic equation to calculate the atomic recoil energy from head-on collisions:

$$T_{\text{max}} = \frac{2(\gamma m v_0)^2}{M} = 2\frac{m}{M}\gamma^2\beta^2 mc^2, \quad (\text{A5})$$

where  $T_{\text{max}}$  is the maximum recoil energy the scattered electron can transfer to an atom;  $m$  denotes electron rest mass;  $M$  is mass of the atom;  $v_0$  and  $c$  represent the speed of the electron and light, respectively; and  $\gamma$  and  $\beta$  are defined by  $\gamma = \sqrt{1 - \beta^2}$  and  $\beta = v_0/c$ . The  $T_{\text{max}}$  for Si and C is calculated to be 204 eV and 476 eV, respectively.

Atomic collision with Compton scattered electrons is the dominant mechanism for displacement defect generation. The other contributions, i.e., photoelectric effect and pair production, are negligible for gamma ray energy of 1.24 eV [41]. The Compton displacement cross sections in Si and C are calculated following Oen and Holmes [51]:

$$\sigma_{\gamma}^{\text{CS}}(E_{\gamma}) = \int_0^{E_0^{\text{max}}} \frac{d\sigma^c(E_{\gamma}, E_0)}{dE_0} \cdot \bar{n}(E_0) dE_0, \quad (\text{A6})$$

where  $E_0$  is the electron recoil energy, and  $E_0^{\text{max}}$ , corresponding to a head-on collision with the gamma incident photon, is calculated via

$$E_0^{\text{max}} = \frac{2E_{\gamma}}{(E_e/E_{\gamma}) + 2}. \quad (\text{A7})$$

$d\sigma^c(E_{\gamma}, E_0)/dE_0$  is the cross section for producing an electron of energy  $E_0$  per unit range of  $E_0$  per atom. It is given by the Klein–Nishina formula [49]:

$$\frac{d\sigma^c(E_{\gamma}, E_0)}{dE_0} = \frac{\pi e^4}{E_e^2} \cdot \frac{1}{E_{\gamma}(E_{\gamma} - E_0)} \left[ 1 + \left( \frac{E_{\gamma} - E_0}{E_{\gamma}} \right)^2 - \frac{2(E_{\gamma} + 1)}{E_{\gamma}^2} + \frac{1 + 2E_{\gamma}}{E_e^2} \left( \frac{E_{\gamma} - E_0}{E_{\gamma}} \right) + \frac{1}{E_{\gamma}(E_{\gamma} - E_0)} \right], \quad (\text{A8})$$

where  $e$  is the electron unit charge,  $E_e$  is the electron rest energy, and  $E_{\gamma}$  is the gamma photon energy.  $\bar{n}(E_0)$  in Eq. (A6) is the average number of electrons with an energy of  $E_0$  determined by the following integral:

$$\bar{n}(E_0) = N_a \int_0^{E_0} \frac{\sigma_d^e(E)}{-dE/dx} dE. \quad (\text{A9})$$

Here  $N_a$  denotes the Avogadro constant, and  $\sigma_d^e(E)$  is the electron displacement cross section.  $-dE/dx$ , the electron stopping power, is expressed as [49]

$$-\frac{dE}{dx} = \frac{2\pi N_a e^4}{m_e \beta^2 c^2} Z^2 \left\{ \ln \frac{m_e \beta^2 c^2 E}{2I(1 - \beta^2)} - [2(1 - \beta^2)^{\frac{1}{2}} - 1 + \beta^2] \ln 2 + 1 - \beta^2 + \frac{1}{8} [1 - (1 - \beta^2)^{\frac{1}{2}}]^2 \right\}, \quad (\text{A10})$$

where  $Z$  is the atomic number, and  $I$  represents the mean excitation potential of the atom ( $I = 1.35 \times 10^{-5} Z \text{ MeV}$ ) [52]. Finally, the displacement defect concentration is calculated using

$$C_{\text{def}} = \Phi_e \sigma C_a, \quad (\text{A11})$$

where  $\Phi_e$  is the total electron flux,  $\sigma$  denotes the Compton displacements cross section, and  $C_a$  is the atomic concentration of the target atom. Assuming an a-SiC film density of  $3.21 \text{ g/cm}^3$  (using the bulk value) and taking into the atomic ratio of Si and C obtained from SIMS analysis, the atomic concentrations of Si and C are calculated to be  $6.6 \times 10^{22} \text{ cm}^{-3}$  and  $3.4 \times 10^{22} \text{ cm}^{-3}$ . The displacement defect concentration is then obtained using Eq. (A11). We note that PECVD-deposited a-SiC likely has a smaller density than bulk crystalline SiC, and therefore our calculated defect concentrations are slightly overestimated.

**Funding.** Defense Threat Reduction Agency (HDTRA1-15-1-0060).

**Acknowledgment.** The authors acknowledge the characterization and fabrication facility of MIT Center of Materials

Science and Engineering and Microsystems Technology Laboratories.

**Disclosures.** The authors declare no conflicts of interest.

## REFERENCES AND NOTES

1. M. Asghari and A. V. Krishnamoorthy, "Silicon photonics: energy-efficient communication," *Nat. Photonics* **5**, 268–270 (2011).
2. D. Marpaung, J. Yao, and J. Capmany, "Integrated microwave photonics," *Nat. Photonics* **13**, 80–90 (2019).
3. D. M. Kita, B. Miranda, D. Favela, D. Bono, J. Michon, H. Lin, T. Gu, and J. Hu, "High-performance and scalable on-chip digital Fourier transform spectroscopy," *Nat. Commun.* **9**, 4405 (2018).
4. S. S. El Nasr-Storey, F. Boeuf, C. Baudot, S. Detraz, J.-M. Fedeli, D. Marris-Morini, L. Olantera, G. Pezzullo, C. Sigaud, and C. Soos, "Silicon photonics for high energy physics data transmission applications," in *11th International Conference on Group IV Photonics (GFP)* (IEEE, 2014), pp. 1–2.
5. V. C. Duarte, J. G. Prata, R. N. Nogueira, G. Winzer, L. Zimmermann, R. Walker, S. Clements, M. Filipowicz, M. Napierala, and T. Nasilowski, "Modular and smooth introduction of photonics in high-throughput communication satellites—perspective of project BEACON," *Proc. SPIE* **11180**, 1118079 (2019).
6. Z. Ahmed, L. T. Cumberland, N. N. Klimov, I. M. Pazos, R. E. Tosh, and R. Fitzgerald, "Assessing radiation hardness of silicon photonic sensors," *Sci. Rep.* **8**, 13007 (2018).
7. A. Kraxner, S. Detraz, L. Olantera, C. Scarcella, C. Sigaud, C. Soos, J. Troska, and F. Vasey, "Investigation of the influence of temperature and annealing on the radiation hardness of silicon Mach-Zehnder modulators," *IEEE Trans. Nucl. Sci.* **65**, 1624–1631 (2018).
8. M. Zeiler, S. S. El Nasr-Storey, S. Detraz, A. Kraxner, L. Olantera, C. Scarcella, C. Sigaud, C. Soos, J. Troska, and F. Vasey, "Radiation damage in silicon photonic Mach-Zehnder modulators and photodiodes," *IEEE Trans. Nuclear Sci.* **64**, 2794–2801 (2017).
9. C. N. Arutt, M. L. Alles, W. Liao, H. Gong, J. L. Davidson, R. D. Schrimpf, R. A. Reed, R. A. Weller, K. Bolotin, and R. Nicholl, "The study of radiation effects in emerging micro and nano electro mechanical systems (M and NEMs)," *Semicond. Sci. Technol.* **32**, 013005 (2016).
10. F. Morichetti, S. Grillanda, S. Manandhar, V. Shutthanandan, L. Kimerling, A. Melloni, and A. M. Agarwal, "Alpha radiation effects on silicon oxynitride waveguides," *ACS Photonics* **3**, 1569–1574 (2016).
11. Q. Du, Y. Huang, O. Ogbuu, W. Zhang, J. Li, V. Singh, A. M. Agarwal, and J. Hu, "Gamma radiation effects in amorphous silicon and silicon nitride photonic devices," *Opt. Lett.* **42**, 587–590 (2017).
12. V. Brasch, Q.-F. Chen, S. Schiller, and T. J. Kippenberg, "Radiation hardness of high-Q silicon nitride microresonators for space compatible integrated optics," *Opt. Express* **22**, 30786–30794 (2014).
13. S. Grillanda, V. Singh, V. Raghunathan, F. Morichetti, A. Melloni, L. Kimerling, and A. M. Agarwal, "Gamma radiation effects on silicon photonic waveguides," *Opt. Lett.* **41**, 3053–3056 (2016).
14. S. Bhandaru, S. Hu, D. Fleetwood, and S. Weiss, "Total ionizing dose effects on silicon ring resonators," *IEEE Trans. Nucl. Sci.* **62**, 323–328 (2015).
15. P. Dumon, R. Kappeler, D. Barros, I. McKenzie, D. Doyle, and R. Baets, "Measured radiation sensitivity of silica-on-silicon and silicon-on-insulator micro-photonic devices for potential space application," *Proc. SPIE* **5897**, 58970D (2005).
16. S. S. El Nasr-Storey, F. Boeuf, C. Baudot, S. Detraz, J. M. Fedeli, D. Marris-Morini, L. Olantera, G. Pezzullo, C. Sigaud, and C. Soos, "Effect of radiation on a Mach-Zehnder interferometer silicon modulator for HL-LHC data transmission applications," *IEEE Trans. Nucl. Sci.* **62**, 329–335 (2015).
17. S. S. El Nasr-Storey, S. Detraz, L. Olantera, C. Sigaud, C. Soos, G. Pezzullo, J. Troska, F. Vasey, and M. Zeiler, "Neutron and X-ray irradiation of silicon based Mach-Zehnder modulators," *J. Instrum.* **10**, C03040 (2015).

18. W. Weber, W. Jiang, and S. Thevuthasan, "Defect annealing kinetics in irradiated 6H-SiC," *Nucl. Instrum. Methods Phys. Res. Sect. B* **166**, 410–414 (2000).
19. G. Brunetti, I. McKenzie, F. Dell'Olio, M. N. Armenise, and C. Ciminelli, "Measured radiation effects on InGaAsP/InP ring resonators for space applications," *Opt. Express* **27**, 24434–24444 (2019).
20. P. Sellin and J. Vaitkus, "New materials for radiation hard semiconductor detectors," *Nuclear Instrum. Methods Phys. Res. Sect. A* **557**, 479–489 (2006).
21. X. Lu, J. Y. Lee, S. Rogers, and Q. Lin, "Optical Kerr nonlinearity in a high-Q silicon carbide microresonator," *Opt. Express* **22**, 30826–30832 (2014).
22. P. Xing, D. Ma, K. J. Ooi, J. W. Choi, A. M. Agarwal, and D. Tan, "CMOS-compatible PECVD silicon carbide platform for linear and nonlinear optics," *ACS Photonics* **6**, 1162–1167 (2019).
23. B.-S. Song, S. Yamada, T. Asano, and S. Noda, "Demonstration of two-dimensional photonic crystals based on silicon carbide," *Opt. Express* **19**, 11084–11089 (2011).
24. Y. Zheng, M. Pu, A. Yi, B. Chang, T. You, K. Huang, A. N. Kamel, M. R. Henriksen, A. A. Jørgensen, and X. Ou, "High-quality factor, high-confinement microring resonators in 4H-silicon carbide-on-insulator," *Opt. Express* **27**, 13053–13060 (2019).
25. T. Fan, H. Moradinejad, X. Wu, A. A. Eftekhar, and A. Adibi, "High-Q integrated photonic microresonators on 3C-SiC-on-insulator (SiCOI) platform," *Opt. Express* **26**, 25814–25826 (2018).
26. A. P. Magyar, D. Bracher, J. C. Lee, I. Aharonovich, and E. L. Hu, "High quality SiC microdisk resonators fabricated from monolithic epilayer wafers," *Appl. Phys. Lett.* **104**, 051109 (2014).
27. J. Cardenas, M. Zhang, C. T. Phare, S. Y. Shah, C. B. Poitras, B. Guha, and M. Lipson, "High Q SiC microresonators," *Opt. Express* **21**, 16882–16887 (2013).
28. I. Chatzopoulos, F. Martini, R. Cernansky, and A. Politi, "High-Q/V photonic crystal cavities and QED analysis in 3C-SiC," *ACS Photonics* **6**, 1826–1831 (2019).
29. D. Allieux, A. Belarouci, D. Hudson, E. Magi, M. Sinobad, G. Beaudin, A. Michon, N. Singh, R. Orobchouk, and C. Grillet, "Toward mid-infrared nonlinear optics applications of silicon carbide microdisks engineered by lateral under-etching," *Photon. Res.* **6**, B74–B81 (2018).
30. M. Radulaski, T. M. Babinec, S. Buckley, A. Rundquist, J. Provine, K. Alassaad, G. Ferro, and J. Vučković, "Photonic crystal cavities in cubic (3C) polytype silicon carbide films," *Opt. Express* **21**, 32623–32629 (2013).
31. G. Calusine, A. Politi, and D. D. Awschalom, "Silicon carbide photonic crystal cavities with integrated color centers," *Appl. Phys. Lett.* **105**, 011123 (2014).
32. A. Lohrmann, T. J. Karle, V. K. Sewani, A. Laucht, M. Bosi, M. Negri, S. Castelletto, S. Praver, J. C. McCallum, and B. C. Johnson, "Integration of single-photon emitters into 3C-SiC microdisk resonators," *ACS Photonics* **4**, 462–468 (2017).
33. D. O. Bracher and E. L. Hu, "Fabrication of high-Q nanobeam photonic crystals in epitaxially grown 4H-SiC," *Nano Lett.* **15**, 6202–6207 (2015).
34. X. Lu, J. Y. Lee, P. X.-L. Feng, and Q. Lin, "High Q silicon carbide microdisk resonator," *Appl. Phys. Lett.* **104**, 181103 (2014).
35. J. T. Robinson, K. Preston, O. Painter, and M. Lipson, "First-principle derivation of gain in high-index-contrast waveguides," *Opt. Express* **16**, 16659–16669 (2008).
36. Q. Li, A. A. Eftekhar, Z. Xia, and A. Adibi, "Azimuthal-order variations of surface-roughness-induced mode splitting and scattering loss in high-Q microdisk resonators," *Opt. Lett.* **37**, 1586–1588 (2012).
37. J. Hu, X. Sun, A. Agarwal, and L. C. Kimerling, "Design guidelines for optical resonator biochemical sensors," *J. Opt. Soc. Am. B* **26**, 1032–1041 (2009).
38. J. Hu, A. Agarwal, L. Kimerling, F. Morichetti, A. Melloni, N. Carlie, and K. Richardson, "Cavity-enhanced photosensitivity in As<sub>2</sub>S<sub>3</sub> chalcogenide glass," in *Bragg Gratings, Photosensitivity, and Poling in Glass Waveguides* (Optical Society of America, 2010), paper BWD2.
39. J. Hu, N. Carlie, N.-N. Feng, L. Petit, A. Agarwal, K. Richardson, and L. Kimerling, "Planar waveguide-coupled, high-index-contrast, high-Q resonators in chalcogenide glass for sensing," *Opt. Lett.* **33**, 2500–2502 (2008).
40. F. De Leonardis, B. Troia, C. E. Campanella, F. Prudenzano, and V. M. Passaro, "Modeling of radiation effects in silicon photonic devices," *IEEE Trans. Nuclear Sci.* **62**, 2155–2168 (2015).
41. J. Kwon and A. T. Motta, "Gamma displacement cross-sections in various materials," *Ann. Nucl. Energy* **27**, 1627–1642 (2000).
42. F. Piao, W. G. Oldham, and E. E. Haller, "The mechanism of radiation-induced compaction in vitreous silica," *J. Non-Cryst. Solids* **276**, 61–71 (2000).
43. B. J. Cowen and M. S. El-Genk, "Point defects production and energy thresholds for displacements in crystalline and amorphous SiC," *Comput. Mater. Sci.* **151**, 73–83 (2018).
44. M. Ediger and P. Harrowell, "Perspective: supercooled liquids and glasses," *J. Chem. Phys.* **137**, 080901 (2012).
45. S. Geiger, Q. Du, B. Huang, M. Y. Shalaginov, J. Michon, H. Lin, T. Gu, A. Yadav, K. A. Richardson, and X. Jia, "Understanding aging in chalcogenide glass thin films using precision resonant cavity refractometry," *Opt. Mater. Express* **9**, 2252–2263 (2019).
46. O. Imagawa, K. Yasuda, and A. Yoshida, "Gamma-ray irradiation effect in amorphous hydrogenated silicon," *J. Appl. Phys.* **66**, 4719–4722 (1989).
47. J. Hu, N. Carlie, L. Petit, A. Agarwal, K. Richardson, and L. C. Kimerling, "Cavity-enhanced IR absorption in planar chalcogenide glass microdisk resonators: experiment and analysis," *J. Lightwave Technol.* **27**, 5240–5245 (2009).
48. A. Yariv, "Universal relations for coupling of optical power between microresonators and dielectric waveguides," *Electron. Lett.* **36**, 321–322 (2000).
49. B. L. Doyle, "Displacement damage caused by gamma-rays and neutrons on Au and Se," SANDIA Report (2014).
50. European Space Components Information Exchange System database.
51. O. S. Oen and D. K. Holmes, "Cross sections for atomic displacements in solids by gamma rays," *J. Appl. Phys.* **30**, 1289–1295 (1959).
52. H. Cember, *Introduction to Health Physics* (Pergamon, 1983).